Journal of Materials Chemistry C

ROYAL SOCIETY OF CHEMISTRY

PAPER

View Article Online
View Journal | View Issue

Cite this: J. Mater. Chem. C, 2023, 11, 3206

Chiral hybrid manganese(II) halide clusters with circularly polarized luminescence for X-ray imaging†

Mengzhu Wang,[a] Xiaoming Wang,[a] Bintao Zhang,[a] Feiyang Li,[a] Haixing Meng,[a] Shujuan Liu*[a] and Qiang Zhao *[ab]

Received 17th December 2022,
Accepted 31st January 2023

DOI: 10.1039/d2tc05379a

rsc.li/materials-c

Chiral organic–inorganic hybrid metal halides with high photoluminescence quantum yield (PLQY) and high luminescence dissymmetry factor (g_{lum}) offer a new platform for multifunctional photoelectric applications. Herein, we report two pairs of chiral organic–inorganic hybrid manganese(II) halide clusters (*R*/*S*-3-aminopyrrolidine dihydrochloride)$_6$(Mn_3Cl_{12})$(Cl)_6$ (***R*/*S*-1**) and (***R*/*S*-1**,2-diaminopropane dihydrochloride)$_3$(Mn_3Cl_{12}) (***R*/*S*-2**). Both of them have high PLQY (more than 42%) under ambient conditions; in particular, the PLQY of ***R*/*S*-2** reached 85%. More importantly, the g_{lum} value of ***R*/*S*-1** ($|g_{lum}|$ = 0.0071) is 3.5 times that of ***R*/*S*-2** ($|g_{lum}|$ = 0.002), showing excellent circularly polarized luminescence (CPL) properties. Through the structural analysis of single crystals, we reveal that the directional arrangement of chiral ligands in manganese cluster molecules has the ability to amplify the CPL properties. Furthermore, based on the excellent luminescence properties of ***R*/*S*-2**, we show examples of their applications as scintillators in X-ray detection and imaging. To our knowledge, this is the first report of chiral manganese(II) halide scintillators. This research provides rational guiding principles for the design and preparation of multifunctional chiral organic–inorganic hybrid metal halides.

Introduction

Materials with circularly polarized luminescence (CPL) have attracted widespread attention due to their wide potential applications for 3D displays, optical data storage, photoelectric devices, asymmetric synthesis, and so on.[1–19] In general, the degree of circular polarization is defined by the strength of left and right circularly polarized light (I_L and I_R).[20] In order to effectively evaluate the intrinsic properties of CPL materials, the luminescence dissymmetry factor (g_{lum}) is defined as the difference between the strength of I_L and I_R divided by their average total luminescence strength, namely $g_{lum} = 2 \times (I_L - I_R)/(I_L + I_R)$.[20] Therefore, the maximum value of the g_{lum} is +2 or −2, which corresponds to the absolute left or right polarized light.[20,21] Unfortunately, most of the developed CPL active materials are limited by the mutual constraints of magnetic and electric dipole transitions, so it is difficult to obtain high photoluminescence quantum yield (PLQY) and high g_{lum} at the same time.[22,23] Chiral organic–inorganic hybrid perovskites combine the excellent optical, electrical and spin properties of chiral and perovskite materials, and provide the ideal platform for designing the next generation of optoelectronic and spintronic devices. So far, a series of chiral lead-based perovskites with high PLQY and high g_{lum} have been constructed.[20] Nevertheless, the toxicity of the lead element and the low stability of lead-based perovskites in the natural state seriously limits the practical application of these materials. The most ideal way to solve this problem is to find low toxicity or non-toxic elements to replace the lead element, while at the same time having the excellent photoelectric properties of lead-based materials.

Due to the advantages of eco-friendliness, low cost and high luminescence quantum efficiency, manganese(II) halides can be used for promising and efficient luminescent materials.[23–26] Their luminescence mechanism comes from the d orbital electron transition in the crystal field.[27–29] At present, manganese-based hybrid halides are widely used in light-emitting diodes, solar cells, photoelectric detection and other fields.[26] However,

[a] State Key Laboratory of Organic Electronics and Information Displays & Jiangsu Key Laboratory for Biosensors, Institute of Advanced Materials (IAM) & Institute of Flexible Electronics (Future Technology), Nanjing University of Posts and Telecommunications, Nanjing 210023, P. R. China. E-mail: iamsjliu@njupt.edu.cn
[b] College of Electronic and Optical Engineering & College of Flexible Electronics (Future Technology), Jiangsu Province Engineering Research Center for Fabrication and Application of Special Optical Fiber Materials and Devices, Nanjing University of Posts and Telecommunications, 9 Wenyuan Road, Nanjing 210023, Jiangsu, P. R. China. E-mail: iamqzhao@njupt.edu.cn

† Electronic supplementary information (ESI) available. CCDC 2219583–2219586. For ESI and crystallographic data in CIF or other electronic format see DOI: https://doi.org/10.1039/d2tc05379a

the discovery of chiral hybrid manganese halides is very scarce, and in particular there is no report on chiral manganese(II) halide clusters. Therefore, the development of novel chiral manganese(II) halide clusters is crucial for the further study of manganese-based halides.

The X-ray imaging technology has important applications in many fields, such as nuclear technology, medical diagnosis, security inspection and space exploration.[30–38] X-ray scintillation, which can convert high-energy X-ray photons into visible light, is the core component of the X-ray detector.[34] Currently, the radioluminescence (RL) signals of almost all scintillators propagate isotropically after generation, causing optical crosstalk between adjacent scintillators and pixels, resulting in degradation of the spatial resolution and imaging quality.[32] Therefore, precise manipulation of the direction of RL propagation of scintillators is expected to fundamentally improve the quality of X-ray imaging. Circularly polarized light has a unique anisotropy that meets the stringent conditions for high level X-ray imaging. Chiral materials with CPL offer a great opportunity for new types of scintillators. Recently, Wang and colleagues demonstrated that chiral perovskite emits circularly polarized radioluminescence when excited under X-rays.[39] To sum up, the development and exploration of chiral scintillators is a hot topic and research focus in this field.

Here, we successfully developed four new manganese(II) halide clusters by combining the structural diversity of chiral organic ligands and the excellent emissive properties of manganese(II), namely (*R*/*S*-3-aminopyrrolidine dihydrochloride)$_6$-(Mn_3Cl_{12})(Cl)$_6$ (***R***/***S*-1**) and (***R***/***S*-1**,2-diaminopropane dihydrochloride)$_3$(Mn_3Cl_{12}) (***R***/***S*-2**). ***R***/***S*-1** and ***R***/***S*-2** emit strong red light with emission wavelengths of 638 nm and 650 nm, respectively. All of them have good stability and high PLQY (more than 42%) under ambient conditions; in particular, the PLQY of ***R***/***S*-2** is more than 85%. The g_{lum} value of ***R***/***S*-1** ($|g_{lum}|$ = 0.0071) is 3.5 times that of ***R***/***S*-2** ($|g_{lum}|$ = 0.002). Through the structural analysis of single crystals, we reveal that the directional arrangement of chiral ligands in manganese cluster molecules has the ability to amplify the CPL properties. Furthermore, based on the excellent luminescence properties of compounds ***R***/***S*-2**, we show examples of their applications as scintillators in X-ray detection and imaging. This research provides rational guiding principles for the design and preparation of multifunctional chiral organic–inorganic hybrid metal halides.

Results and discussion

Synthesis and characterization

Detailed synthesis routes of the manganese(II) halide clusters are shown in Fig. S1 in the ESI.† Two pairs of enantiomorphic chiral amino hydrochlorides reacted with manganese chloride in methanol at 60 °C to form two pairs of enantiomorphic manganese(II) halide clusters (R/S-$C_4H_{12}N_2)_6(Mn_3Cl_{12})(Cl)_6$ (***R***/***S*-1**) (CCDC, 2219583/2219584†) and (R/S-$C_3H_{12}N_2)_3(Mn_3Cl_{12})$ (***R***/***S*-2**) (CCDC, 2219585/2219586†) (Fig. 1).

Crystal structure and photophysical properties of *R*/*S*-1 and *R*/*S*-2

The single crystal structures of these manganese(II) halide clusters were obtained by single-crystal X-ray diffraction (SCXRD) analysis. The results of X-ray diffraction analysis show that ***R*-1**, ***S*-1**, ***R*-1** and ***S*-2** exhibit the space group of *R*32, *R*3, *C*2 and *C*2, respectively, all of which belong to the chiral space group. Although all of them are chiral manganese(II) cluster structures, ***R***/***S*-1** consists of six chiral $[R/S\text{-}C_4H_{12}N_2]^{2-}$ cations, one $[Mn_3Cl_{12}]^{6-}$ unit and six free chloride ions, while ***R***/***S*-2** is composed of three chiral $[R/S\text{-}C_3H_{12}N_2]^{2-}$ cations and one $[Mn_3Cl_{12}]^{6-}$ unit. Their intramolecular interactions are shown in Fig. S2 (ESI†). This difference in composition affects the luminescence properties of these materials, as we will discuss later. The detailed SCXRD data of ***R***/***S*-1** and ***R***/***S*-2** are listed in Table S1 in the ESI.† The powder XRD peaks of all manganese(II) halide clusters are highly consistent with the

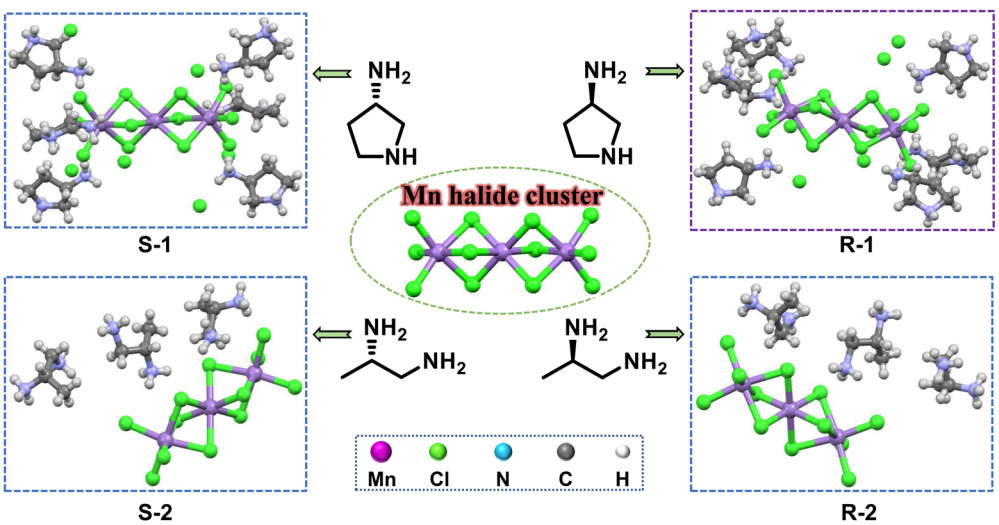

Fig. 1 Schematic diagram of the crystal structures of ***R***/***S*-1** and ***R***/***S*-2**.

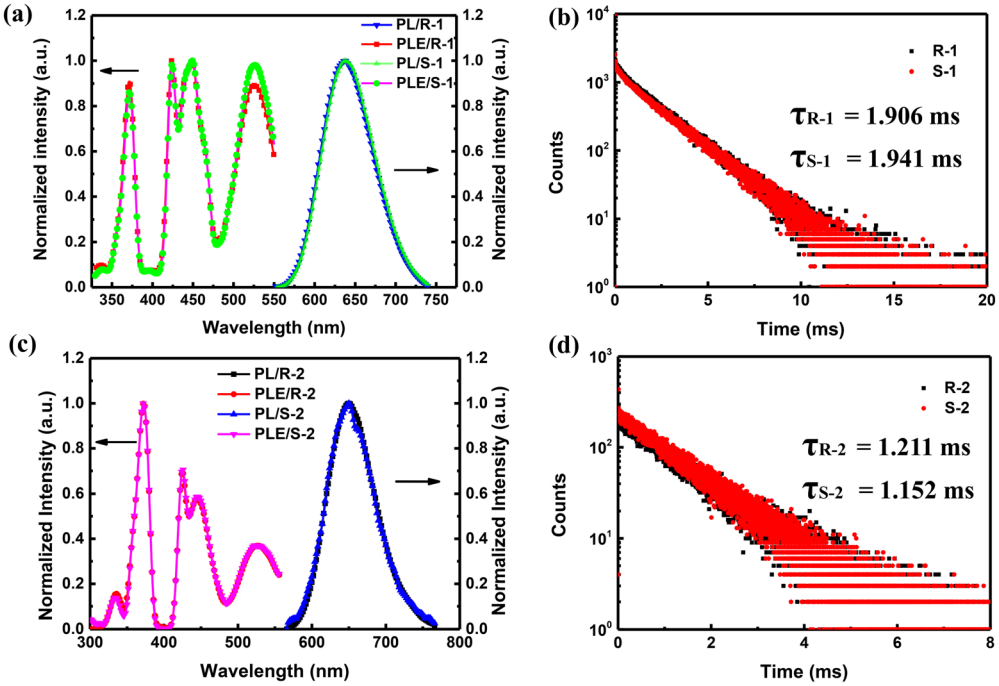

Fig. 2 (a) Excitation and emission spectra of ***R*/*S*-1**. (b) The time-resolved PL decay curves of ***R*/*S*-1** at 298 K. (c) Excitation and emission spectra of ***R*/*S*-2**. (d) The time-resolved PL decay curves of ***R*/*S*-2** at 298 K.

corresponding simulated SCXRD data (Fig. S3, ESI†), which proves their high purity. At the same time, their thermogravimetric analysis curves are shown in Fig. S4 (ESI†), and the thermal decomposition temperature of these halide clusters is higher than 280 °C, proving great thermal tolerance. More importantly, all manganese(II) halide clusters can keep their structures from being destroyed after being placed under natural conditions for a month, which indicates that they are more stable than lead-base and other manganese-based perovskite materials.

The luminescence properties of these manganese(II) halide clusters were studied in detail. These clusters were characterized using steady state photoluminescent (PL) and excitation (PLE) spectra. As shown in Fig. 2a and c, between 300 nm and 550 nm, ***R*/*S*-1** and ***R*/*S*-2** exhibit three dominant excitation peaks. The PLE spectrum of ***R*/*S*-1** includes several bands at 360, 372, 424, 448, and 525 nm, which correspond to electronic transitions from the $^6A_1$ ground state of Mn^{2+} ions to $^4E_g(D)$, $^4T_{2g}(D)$, $[^4A_{1g}(G),^4E_g]$, $^4T_{2g}(G)$, and $^4T_{1g}(G)$, respectively. The peak emission is located around 638 nm, with a full width at half-maximum (FWHM) of 75 nm, which occurs due to the $^4T_1(G)$ to $^6A_1$ radiative transition of octahedrally coordinated Mn^{2+} in the inorganic framework $[Mn_3Cl_{12}]^{6-}$. In Fig. 2b, the excitation bands of ***R*/*S*-2** are located at 360, 372, 424, 445, and 526 nm, which are attributed to electronic transitions of Mn^{2+} from the ground state to $^4E_g(D)$, $^4T_{2g}(D)$, $[^4A_{1g}(G),^4E_g]$, $^4T_{2g}(G)$, and $^4T_{1g}(G)$, respectively. There are emission peaks of 650 nm as well as the FWHM of 75 nm, and these correspond to the $^4T_1(G)$-$^6A_1$ radiative transition of Mn^{2+} in the inorganic framework $[Mn_3Cl_{12}]^{6-}$ units. The position of the Mn^{2+} emission peak depends on the strength of the crystal field in which the Mn^{2+} ion stays, according to the general theory of d-ion emission.[21] For these four clusters, their luminescent centers are derived from the octahedrally coordinated Mn^{2+} ions in the $[Mn_3Cl_{12}]^{6-}$. Their crystal field strength is relatively large and the $^4T_1$–$^6A_1$ energy level is reduced, resulting in Mn^{2+} ions exhibiting red emission with low energy.

Meanwhile, the luminescence lifetimes of ***R*/*S*-1** under 450 nm excitation are 1.906 ms and 1.941 ms, respectively (Fig. 2b), while those of ***R*/*S*-2** under 375 nm excitation are 1.211 ms and 1.152 ms, respectively (Fig. 2d). The long luminescence lifetimes indicated the spin-forbidden d–d transitions in the center of Mn^{2+}. The similar curve shape can further confirm the emission resulting from the $^4T_1$–$^6A_1$ transition feature of the Mn^{2+} ion. Compared to ***R*/*S*-2**, ***R*/*S*-1** contains twice the number of chiral ligands, as well as six additional free chloride ions. Due to the heavy atom effect of the free chlorine ions, the luminescence lifetimes of ***R*/*S*-1** are relatively long. The PLQY of ***R*/*S*-1** is 42.5% and 44.2%, respectively, which is far lower than 86.3% and 85.5% of ***R*/*S*-2**, respectively. In the ESI,† Fig. S5 shows the measured spectra. The PLQY of all four crystals is higher than 42%, which may be related to the specific Mn^{2+} ion environment in the crystal structures. The PLQY of ***R*/*S*-1** is much lower than that of ***R*/*S*-2**, which is also due to the effect of free chloride ions.

CPL properties of *R*/*S*-1 and *R*/*S*-2

To demonstrate the chiral optical activity of the manganese(II) clusters, solid state ultraviolet visible (UV-Vis) absorption spectroscopy and circular dichroism (CD) spectra were measured.

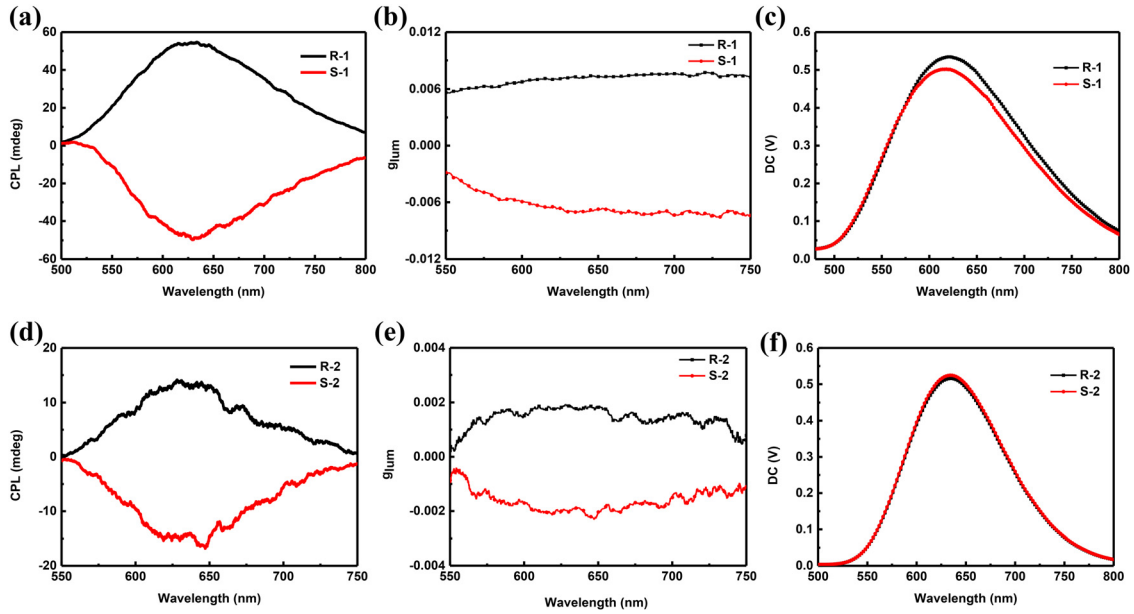

Fig. 3 The CPL spectra of ***R*/*S*-1** (a) and ***R*/*S*-2** (d). The g_{lum} of ***R*/*S*-1** (b) and ***R*/*S*-2** (e). The DC spectra of ***R*/*S*-1** (c) and ***R*/*S*-2** (f).

Fig. S6 (ESI†) shows the CD spectra and UV-Vis absorption spectra of ***R*/*S*-1** and ***R*/*S*-2**. In the same band range, the CD signals of ***R*-1** and ***S*-1** were opposite. Similarly, ***R*-2** and ***S*-2** display mirror symmetry of CD signals. The Cotton effect of the hybrid manganese(II) clusters is affected by the chiral ammonium cations.[40]

To investigate the CPL properties of this new series of manganese(II) clusters, we measured their circularly polarized luminescence spectra. These cluster compounds exhibit high-performance CPL emissions. As shown in Fig. 3a and d, in their CPL emission spectra, polycrystalline ***R*/*S*-1** and ***R*/*S*-2** emerge mirror image outlines. The g_{lum} values of polycrystalline ***R*-1**, ***S*-1**, ***R*-2**, and ***S*-2** at their maximum emission wavelengths are $+7.1 \times 10^{-3}$, -7.1×10^{-3}, $+2.0 \times 10^{-3}$, and -2.0×10^{-3}, respectively (Fig. 3b and e). The g_{lum} values of ***R*/*S*-1** are 3.5 times those of ***R*/*S*-2**. The CPL data of all the compounds after storing in natural conditions for one month were basically consistent with the original data. Compared with the reported

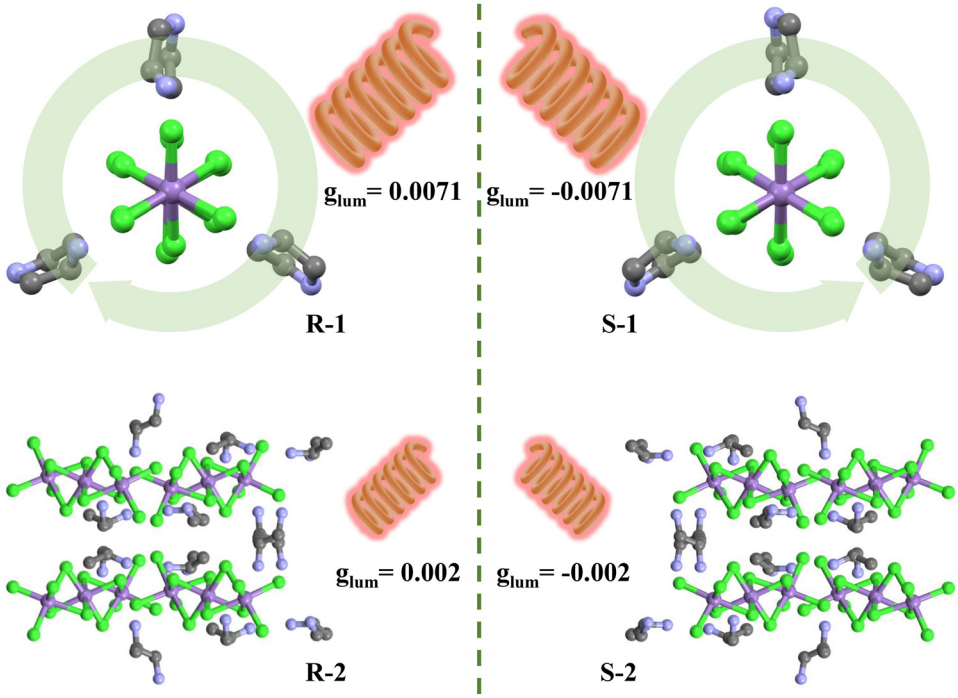

Fig. 4 The chiral schematic diagram of the manganese(II) clusters is magnified by the directional arrangement of the chiral ligands.

chiral lead-based and manganese-based hybrid materials, the high stability of these manganese(II) clusters is worth expecting. This suggests that chiral manganese(II) clusters have broad practical application prospects. This is the first report on chiral manganese(II) clusters with CPL properties, as far as we know. These new findings point out a direction for the development of high-performance CPL materials.

Mechanism of CPL properties

In general, the degree of chirality is higher in low-dimensional structures. For ***R*/*S*-1** and ***R*/*S*-2**, they are zero-dimensional chiral hybrid manganese(II) clusters. They are all composed of chiral ligands and an inorganic framework ($[Mn_3Cl_{12}]^{6-}$) through hydrogen bonds. For inorganic framework $[Mn_3Cl_{12}]^{6-}$, it only acts as the luminescence center of the compounds and has no intrinsic chiral characteristics. Therefore, the CPL of these four compounds results from the induction of the luminescent center by the chiral ligands. By single crystal analysis of these compounds, we found that the chiral ligands uniformly surround the manganese clusters in ***R*/*S*-1**, but not in ***R*/*S*-2** (Fig. 4). We believe that the directional arrangement of ligands in ***R*/*S*-1** is conducive to the amplification of the chirality of the material, resulting in high g_{lum} value. This provides a new way to amplify the chirality of organic–inorganic hybrid materials.

X-Ray detection and imaging

In view of the excellent photophysical properties of ***R*/*S*-2**, we explored their application as scintillators. Under X-ray irradiation, ***R*/*S*-2** display bright red-emission. The radioluminescence (RL) spectra are basically coincident with the PL spectra (Fig. S7, ESI†), indicating that X-ray scintillation luminescence is the same as PL. Furthermore, Fig. 5a shows the X-ray attenuation efficiency of ***R*/*S*-2** as a function of film thickness at the X-ray photon energy of 22 keV, which is the dominant X-ray energy produced by our X-ray tube.[17] We further evaluate the efficiency of ***R*/*S*-2** in converting high-energy X-rays into visible light. Herein, in order to accurately quantify the steady-state X-ray to visible light conversion efficiency of ***R*/*S*-2**, a commercial scintillator with a known light yield of 24 900 photons per MeV, LuAG:Ce, was selected as the reference standard. In Fig. 5f, the light yield of ***R*/*S*-2** was determined to be 14 532 and 13 638 photons per MeV, respectively. The lowest detection limit (LOD) is also a key parameter in determining the lowest dose rate required for testing.[17] Here, ***R*-2** is used as an example, and its minimum detection limit is confirmed to be 90.5 $nGy_{air}\ s^{-1}$ (Fig. 5d) when the signal-to-noise ratio (SNR) is equal to 3, which is 60 times lower than the dose rate required for X-ray diagnosis (5.5 $\mu Gy_{air}\ s^{-1}$). In view of the excellent performance of the clusters, we further demonstrate the potential of functional X-ray imaging. In Fig. 5g and h, the

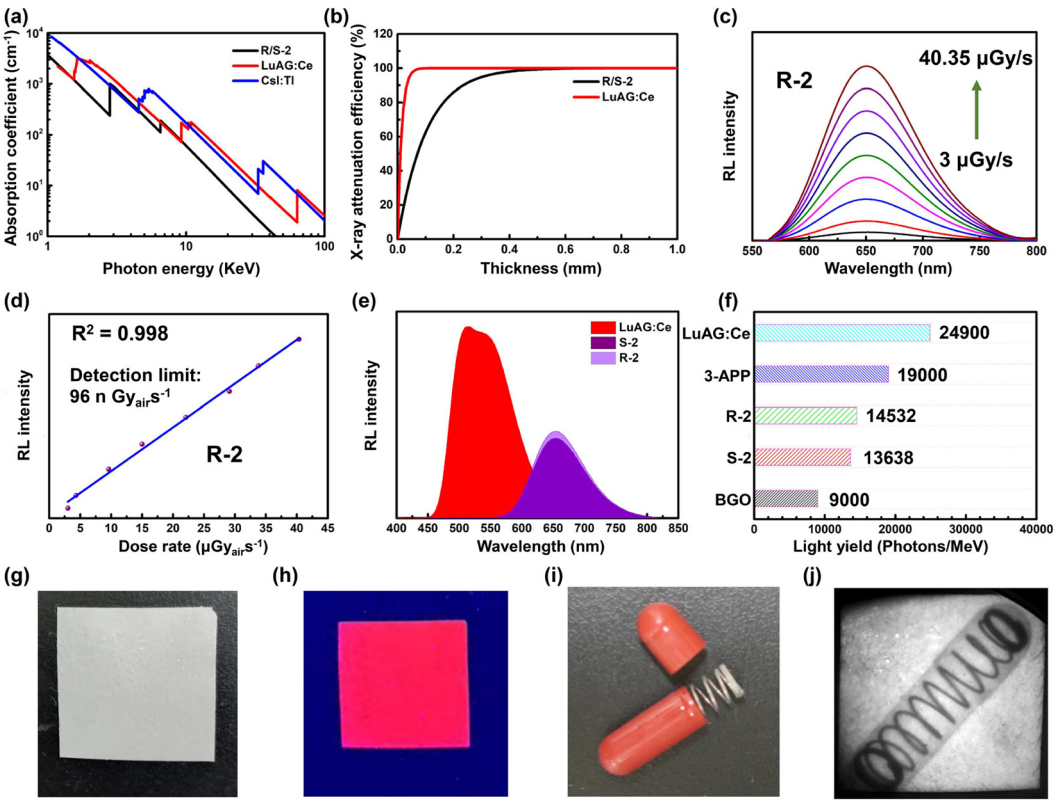

Fig. 5 (a) Absorption coefficients of ***R*/*S*-2**, LuAG:Ce and CsI:Tl as a function of photon energy. (b) X-ray attenuation efficiencies of ***R*/*S*-2** scintillator film thickness. (c) RL spectra of the ***R*-2** with dose rate-dependence. (d) Detection limit (DL) of the ***R*-2**. (e) RL spectra of ***R*/*S*-2** and LuAG:Ce under the same conditions. (f) Comparison of the light yield of ***R*/*S*-2** and some well-acknowledged scintillators. (g) A photo of the ***R*-2** scintillation screen. (h) A photo of the ***R*-2** scintillation screen under 365 nm excitation light. (i) A photo of the metal spring and capsule. (j) X-ray image of a metal spring.

scintillation screen was prepared by effectively mixing ***R*-2** with polymer (PMMA). As shown in Fig. 5j, the metal spring inside the capsule can be clearly imaged. The modulation transfer function (MTF) extracted from the X-ray image of the slanted edge is also used to confirm the spatial resolution of the ***R*-2** screen.[25] In Fig. S7 in the ESI,† the X-ray images of the slanted edge and the thin lead slice with a sharp edge are shown. As shown in Fig. S8 (ESI†), when MTF equals 0.2, the spatial resolution of the ***R*-2** screen is defined as 5.4 lp mm^{-1}, which is consistent with the 5.4 lp mm^{-1} observed in the X-ray image of the test pattern plate. To our knowledge, this is the first report of a chiral manganese(II) halide scintillator. Our research provides a new perspective for the exploitation of novel scintillation materials.

Conclusions

In summary, two pairs of enantiomorphic organic–inorganic hybrid manganese(II) halide clusters have been successfully designed and synthesized utilizing different chiral diamine ligands. They showed excellent stability and high PLQY. More importantly, the g_{lum} values of ***R*/*S*-1** ($|g_{lum}|$ = 0.0071) are 3.5 times those of ***R*/*S*-2** ($|g_{lum}|$ = 0.002), showing excellent CPL properties. Through the structural analysis of single crystals, we reveal that the directional arrangement of chiral ligands in manganese cluster molecules has the ability to amplify the CPL properties. Furthermore, based on the excellent luminescence properties of compounds ***R*/*S*-2**, we show examples of their applications in X-ray detection and imaging as scintillators. To our knowledge, this is the first report of chiral manganese(II) halide scintillators. This research provides rational guiding principles for the design and preparation of multifunctional chiral organic–inorganic hybrid metal halides.

Conflicts of interest

There are no conflicts to declare.

Acknowledgements

This work was supported by the National Funds for Distinguished Young Scientists (61825503), the National Natural Science Foundation of China (61775101 and 62005241), the Postgraduate Research & Practice Innovation Program of Jiangsu Province (No. KYCX20_0749) and National Key R&D Program of China (2022YFA1200094).

Notes and references

1 Y. J. Deng, M. Z. Wang, Y. L. Zhuang, S. J. Liu, W. Huang and Q. Zhao, *Light: Sci. Appl.*, 2021, **10**, 76.
2 Z. L. Gong, X. F. Zhu, Z. H. Zhou, S. W. Zhang, D. Yang, B. Zhao, Y. P. Zhang, J. P. Deng, Y. X. Cheng, Y. X. Zheng, S. Q. Zang, H. Kuang, P. F. Duan, M. J. Yuan, C. F. Chen, Y. S. Zhao, Y. W. Zhong, B. Z. Tang and M. H. Liu, *Sci. China: Chem.*, 2021, **64**, 2060–2104.
3 C. Ren, T. H. Zhao, Y. H. Shi and P. F. Duan, *Chem. Commun.*, 2023, **59**, 567–570.
4 C. Li, Y. Sang, X. Jin, P. Duan and M. Liu, *Angew. Chem., Int. Ed.*, 2022, **61**, e202206332.
5 T. H. Zhao, D. J. Meng, Z. J. Hu, W. J. Sun, Y. L. Ji, J. L. Han, X. Jin, X. C. Wu and P. F. Duan, *Nat. Commun.*, 2023, **14**, 81.
6 Y. H. Zhou, A. W. Zhang, R. J. Huang, Y. H. Sun, Z. J. Chen, B. S. Zhu and Y. X. Zheng, *J. Mater. Chem. C*, 2023, **11**, 1329–1335.
7 M. X. Mao, S. Xing, Y. P. Zhang, Z. Z. Qu, L. Yuan, J. J. Hu, X. J. Liao, Y. Zhao and Y. X. Zheng, *J. Mater. Chem. C*, 2022, **10**, 8650–8656.
8 X. Y. Chen, J. K. Li, W. L. Zhao, C. Z. Du, M. Li, C. F. Chen and X. Y. Wang, *J. Mater. Chem. C*, 2023, **11**, 893–897.
9 L. Meng, Z. Q. Li, K. Tang, J. Y. Shao, Z. L. Chen and Y. W. Zhong, *J. Mater. Chem. C*, 2023, **11**, 676–684.
10 P. X. Guo, R. Q. Jin, M. Z. Wang, Q. He, C. H. Cai, Q. Zhao and W. F. Bu, *J. Organomet. Chem.*, 2021, **931**, 121616.
11 A. Y. Zheng, T. H. Zhao, C. Xiao, X. Jin and P. F. Duan, *J. Mater. Chem. C*, 2022, **10**, 13084–13092.
12 T. G. Dong, Z. G. Wu, F. L. Li, J. Z. Wang, Y. X. Zheng and L. W. Yu, *Adv. Opt. Mater.*, 2022, **10**, 2201105.
13 J. M. Han, S. Guo, H. Lu, S. J. Liu, Q. Zhao and W. Huang, *Adv. Opt. Mater.*, 2018, **6**, 1800538.
14 Y. P. Zhang and Y. X. Zheng, *Dalton Trans.*, 2022, **51**, 9966–9970.
15 J. M. Han, H. Lu, Y. Xu, S. Guo, X. K. Zheng, P. Tao, S. J. Liu, X. W. Zhang and Q. Zhao, *J. Organomet. Chem.*, 2020, **915**, 121240.
16 J. M. Han, S. Guo, J. Wang, L. W. Wei, Y. L. Zhuang, S. J. Liu, Q. Zhao, X. W. Zhang and W. Huang, *Adv. Opt. Mater.*, 2017, **5**, 1700359.
17 J. H. Li, Y. F. Xie, Z. Y. Feng, C. T. Zhang, H. L. Zhang, X. Chen and G. Zou, *J. Mater. Chem. C*, 2022, **10**, 16556–16563.
18 X. H. Zhao, X. Z. Hu, M. E. Sun, X. M. Luo, C. Zhang, G. S. Chen, X. Y. Dong and S. Q. Zang, *J. Mater. Chem. C*, 2022, **10**, 3440–3446.
19 Z. B. Liang, X. Chen, X. J. Liao, J. J. Li, Y. Yang, C. F. Wang, Y. X. Zheng and S. Chen, *J. Mater. Chem. C*, 2022, **10**, 12644–12651.
20 J. Chen, S. Zhang, X. Pan, R. Li, S. Ye, A. K. Cheetham and L. Mao, *Angew. Chem., Int. Ed.*, 2022, **61**, e202205906.
21 J. Han, D. Yang, X. Jin, Y. Jiang, M. Liu and P. Duan, *Angew. Chem., Int. Ed.*, 2019, **58**, 7013–7019.
22 Y. Wang, D. Niu, G. Ouyang and M. H. Liu, *Nat. Commun.*, 2022, **13**, 1710.
23 X. M. Huang, Y. Y. Qin, P. F. She, H. X. Meng, S. J. Liu and Q. Zhao, *Dalton Trans.*, 2021, **50**, 8831–8836.
24 H. X. Meng, W. J. Zhu, Z. J. Zhou, R. Y. Zhou, D. Yan, Q. Zhao and S. J. Liu, *J. Mater. Chem. C*, 2022, **10**, 12286–12291.
25 X. Liu, R. Li, X. Xu, Y. Jiang, W. Zhu, Y. Yao, F. Li, X. Tao, S. Liu, W. Huang and Q. Zhao, *Adv. Mater.*, 2022, 2206741.
26 X. Liu, Y. Jiang, F. Li, X. Xu, R. Li, W. Zhu, J. Ni, C. Ding, S. Liu and Q. Zhao, *Adv. Optical Mater.*, 2022, 2202169.

27 H. Meng, W. Zhu, F. Li, X. Huang, Y. Qin, S. Liu, Y. Yang, W. Huang and Q. Zhao, *Laser Photonics Rev.*, 2021, **15**, 2100309.
28 P. Tao, S. J. Liu and W.-Y. Wong, *Adv. Opt. Mater.*, 2020, **8**, 2000985.
29 Q. Sun, S. Wang, C. Zhao, J. Leng, W. Tian and S. Jin, *J. Am. Chem. Soc.*, 2019, **141**, 20089–20096.
30 N. K. Nandha and A. Nag, *Chem. Commun.*, 2018, **54**, 5205–5208.
31 W. J. Mir, M. Jagadeeswararao, S. Das and A. Nag, *ACS Energy Lett.*, 2017, **2**, 537–543.
32 K. Han, K. Sakhatskyi, J. Jin, Q. Zhang, M. V. Kovalenko and Z. Xia, *Adv. Mater.*, 2022, **34**, 2110420.
33 B. H. Li, Y. Xu, X. L. Zhang, K. Han, J. C. Jin and Z. G. Xia, *Adv. Opt. Mater.*, 2022, **10**, 2102793.
34 Y. Y. Ma, Y. R. Song, W. J. Xu, Q. Q. Zhong, H. Q. Fu, X. L. Liu, C. Y. Yue and X. W. Lei, *J. Mater. Chem. C*, 2021, **9**, 9952–9961.
35 Y. Zhou, J. Chen, O. M. Bakr and O. F. Mohammed, *ACS Energy Lett.*, 2021, **6**, 739–768.
36 Y. L. Song, L. Q. Li, M. W. Hao, W. H. Bi, A. R. Wang, Y. F. Kang, H. M. Li, X. H. Li, Y. J. Fang, D. R. Yang and Q. F. Dong, *Adv. Mater.*, 2021, **33**, 2103078.
37 L. Y. Lian, M. Y. Zheng, W. Z. Zhang, L. X. Yin, X. Y. Du, P. Zhang, X. W. Zhang, J. B. Gao, D. L. Zhang, L. Gao, G. D. Niu, H. S. Song, R. Chen, X. Z. Lan, J. Tang and J. B. Zhang, *Adv. Sci.*, 2020, **7**, 2000195.
38 M. Y. Zhang, J. S. Zhu, B. Yang, G. D. Niu, H. D. Wu, X. Zhao, L. X. Yin, T. Jin, X. Y. Liang and J. Tang, *Nano Lett.*, 2021, **21**, 1392–1399.
39 M. Li, Y. M. Wang, L. W. Yang, Z. F. Chai, Y. X. Wang and S. A. Wang, *Angew. Chem., Int. Ed.*, 2022, **61**, e202208440.
40 B. Wang, C. Wang, Y. Chu, H. Zhang, M. Sun, H. Wang, S. Wang and G. Zhao, *J. Alloys Compd.*, 2022, **910**, 164892.

